基于超透镜阵列的平面人工复眼研究

周力,张晓虎,林晓钢,高潮,郭永彩

（重庆大学 光电工程学院 光电技术与系统教育部重点实验室, 重庆 400044）

摘　要：为了实现轻量化、集成化与大视场的光学成像系统,提出了一种基于超透镜阵列的平面化人工复眼结构。该结构使用基于几何相位原理的不同取向二氧化钛纳米柱结构来实现电磁波调控,使得超透镜阵列面与复眼的像面均为平面,不需要传统曲面复眼所需要的非球面加工。在传统超透镜聚焦相位的基础上叠加倾斜相位,能够较好地抵消光学系统非近轴区域光线离轴照明对成像质量的影响,实现大视场复眼的效果。所设计的复眼主要由一个 11×11 的超透镜阵列组成,总体尺寸仅为 165 μm×165 μm,总体高度为 18.6 μm,视场角可达 140°×140°。仿真结果表明:光线以较大离轴角(50°)照明的情况下,所提出的复眼结构仍能实现较好的成像效果。

关键词：超透镜阵列；人工复眼；超表面；离轴成像；轻量化；平面结构；大视野

中图分类号：Q632；TB853.9　　　　**文献标识码**：A　　　　**doi**：10.3788/gzxb20215006.0623001

A Planar Artificial Compound Eye Based on Metalens Array

ZHOU Li, ZHANG Xiaohu, LIN Xiaogang, GAO Chao, GUO Yongcai

（*Key Laboratory of Optoelectronic Technology and Systems of the Education Ministry of China*, *College of Optoelectronic Engineering*, *Chongqing University*, *Chongqing* 400044, *China*）

Abstract：In order to realize an optical imaging system with light-weight, integration and large field of view, a planar artificial compound eye structure based on the utilization of a metalens array is proposed. It uses TiO_2 nanopillars with different orientation angles to manipulate the electro-magnetic wave based on the grometric phase principles. It makes the surface of the metalens array and the image plane both planar, and does not need the non-spherical processing required by the traditional curved compound eyes. With the superposition of the off-axis phase onto the traditional matalens' focusing phase, the effect produced by the illumination of the non-paraxial light beams on the imaging quality is effectively canceled and a large field of view is achieved. The designed compound eye is mainly composed of an array of 11×11 metalenses. It has the size of the 165 μm×165 μm and overall height of 18.6 μm, with the field of view of 140°×140°. The simulation results indicates that the the proposed compound eye structure achieves good image quality even under the illumination at a large off-axis angle (50°).

Key words：Metalens array；Artificial compound eye；Metasurface；Off-axis imaging；Light-weight；Planar structure；Large field of view

OCIS Codes：230.1950；050.1380；050.1965；050.5080；050.6624；110.7348

http∶// www .photon .ac .cn

0 Introduction

The traditional optical systems are usually single-aperture systems which are consisted of bulky optical elements with elaborate designs to eliminate aberrations and improve imaging qualities, such as doublet lenses and aspheric lenses. Benefitting from those excellent properties, they are widely used in many scenarios. However, some applications of rapid development (like drones and endoscopy imaging) in recent years have raised higher demands for the imaging system, such as light weight, small size, and large Field Of View (FOV). The bulky volumes and heavy weights of traditional optical systems make them difficult to be miniaturized and integrated. A new methodology which can simultaneously realize the miniaturization and large FOV of the image systems is highly expected in the optical field.

To achieve such goals, Artificial Compound Eyes (ACEs) were developed based on the structures of the biotic compound eyes for their features including compact structure and large FOV[1-3]. The ACEs were typically composed of a Micro Lens Array (MLA) with space-variant field angles to transfer different portions of the overall FOV independently. By combining the obtained subimages, a large FOV could be achieved. Compared with traditional single-aperture systems, the imaging lenses of the ACE had a much smaller size both radially and axially, making it convenient for the miniaturization of the optical system. In general, current ACE structures can be classified into the Three-Dimensional(3D) ACEs[4-6] and the planar ACEs[7-9]. A 3D ACE fully realizes the characteristics of biotic compound eyes with a curved lens plane, which allows the micro lenses to be rotated and aimed for different directions. However, the original structure produces a curved image plane, making the subimages difficult to be collected with a planar CCD or CMOS detector. To handle this problem, a micro-lens array with radially decreasing focal length is proposed to ensure that the subimages are generated precisely on the detector plane[10]. Another solution is adding an intermediate system, such as optical fibers or lenses, to transfer the optical path and produce a planar image plane. The planar ACEs, of which both the lens plane and the image plane are planar, are easier to be designed and realized than the 3D ACEs, while they have a lower FOV compared with the 3D ACEs. To increase the FOV of the planar ACEs, different methods are adopted, such as the utilization of optical prisms to deflect light beams[11], or introducing of multiple layers of MLA[12]. Although the aforementioned methods could handle the drawbacks of ACE, the introduced components decrease the system's integration level and increase the system complexity. A new ACE structure that simultaneously guarantees a large FOV, small size and simple structure is highly desired in the ACE domain.

In this work, a planar ACE structure is proposed based on the utilization of metalenses. Metasurface lens (metalens)[13-15], which is a planar device with sub-wavelength phase-modulation structures, is an important branch of application of the metasurfaces[16]. The Metalens Array (MA) of the proposed ACE is composed of metalenses with different off-axis angles to transfer different portions of the object space. Benefitting from the multi-function properties, metalenses can deflect the incident light's axis without self-rotation nor additional devices, while maintaining the focusing function. Here, a planar ACE is designed with the size of 165 μm×165 μm and overall height of 18.6 μm. The simulation result reveals that the overall FOV of the designed planar ACE can reach 140°×140°, with nearly constant resolution (FWHM(Full-Width-Half-Maximum)＝0.74±0.01 μm) in all directions. Compared with some previous results[17-18], the proposed planar ACE has a smaller overall size and a simplified structure. Our work provides a new approach for designing the planar ACE, promoting its application in fast positioning, monitoring, medical and industrial fields.

1 Design process of ACE

1.1 Schematic of the ACE

The detailed layout of the proposed planar ACE is shown in Fig.1. It comprises a single layer of planar MA, which is usually supported by a layer of transparent base (which is silicon dioxide (SiO_2) in this work) and a light receiver focal plane to collect the generated subimages. The MA is composed of metalenses to generate the subimages of different portions of the object field. The metalenses are designed with a side length $d＝10.2$ μm and height $h＝0.6$ μm. The FOV of a single metalens φ reaches 40° according to the simulation results, and it is here taken as $\varphi＝40°$. In addition to focusing, each metalens is designed with an off-axis angle α, which

represents its off-axis angle in the object space. When the incident direction is parallel to the metalens' off-axis direction, the transmitted light beams are normally focused onto the focal plane. Thus, a portion of the object field $(\alpha-\varphi/2, \alpha+\varphi/2)$ is transferred successfully. The inter-ommatidia angle $\Delta\alpha$ is defined as the difference of the off-axis angles between adjacent metalenses. With $\Delta\alpha$ set smaller than φ to eliminate blind areas, the overall FOV of the MA Φ can reach $\pm(\alpha_{max}+\varphi/2)$, where α_{max} is the maximum off-axis angle. To prevent crosstalk, optical isolators should be added between adjacent channels[19]. In this design, with $\Delta\alpha=10°$, $\alpha_{max}=50°$, and $\varphi=40°$, an array of $11\times11=121$ metalenses can cover the overall field $(-70°, 70°)$. The adjacent metalenses are distributed with an interval $D=15$ μm to avoid conflicts between adjacent metalenses, resulting in the ACE's size of 165 μm $\times$ 165 μm. The overall height of the proposed ACE, which is mainly determined by the height of the metalenses ($h=0.6$ μm) and the focal length ($f=18$ μm), is 18.6 μm (the overall height does not include the thickness of the supporting SiO_2 base, which depends on the manufacture technology in practical). Here, because the focal points of the metalenses are on a flat plane, the image plane of the proposed ACE is also planar, making it much easier for the detectors to collect the produced subimages without additional converting components or curving process.

(a) The overall scheme of the ACE   (b) Details of a metalens
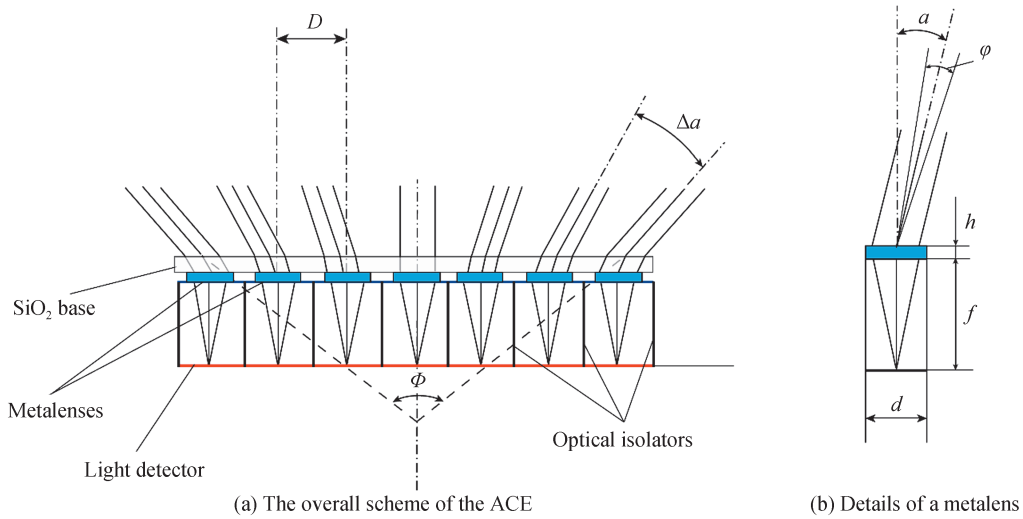
Φ: The overall FOV of the planar ACE; D: The interval between adjacent metalenses; φ: FOV of a single metalens; $\Delta\alpha$: The difference of the off-axis angles between adjacent metalenses; α: The off-axis angle of a metalens; d: The side length of a metalens; h: Height of the metalenses; f: Focal length of the metalenses

Fig. 1   The scheme of the planar ACE

1.2   The optical performance of the subwavelength structure

The metalenses used to construct the MA is a newly developed planar lens that controls light based on the geometric phase. The geometric phase, also named as Pancharatnam-Berry (PB) phase, is always frequency-independent and can be conveniently implemented through the rotation of the nano-structures[20-22]. In this design, the metalenses are constructed by nanopillars with space-variant orientation angles (Fig. 2(a)) to modulate the transmitted phase and realize off-axis focusing. Titanium dioxide (TiO_2) is an ideal material to construct such a metalens because of its high refractive index with near-zero imaginary parts and negligible absorption across the visible range[23]. In order to obtain good performance, the geometric dimensions of the rectangle nanopillars, including its height, length, width, and period, are specifically optimized based on the cross-polarization amplitude and phase responses, which are simulated using the Computer Simulation Technology (CST) Microwave Studio. As a result, the height, length, width, and period shown in Fig.2(a) are chosen as 0.6 μm, 0.2 μm, 0.09 μm and 0.3 μm, respectively.

Under the normal incidence of Left Circular Polarized (LCP) light at 467.5 nm wavelength, the amplitude and phase response of the transmitted cross-polarization light, which in this case is the Right Circular Polarized (RCP) light, is calculated and shown in Fig.2(b). The amplitude is above 99% and the phase is almost in a linear relation with the rotation angle, which agrees with the geometric phase anticipation. Fig. 2(c) shows the phase shift of the transmitted cross-polarization light produced by nanopillars with different orientation angles
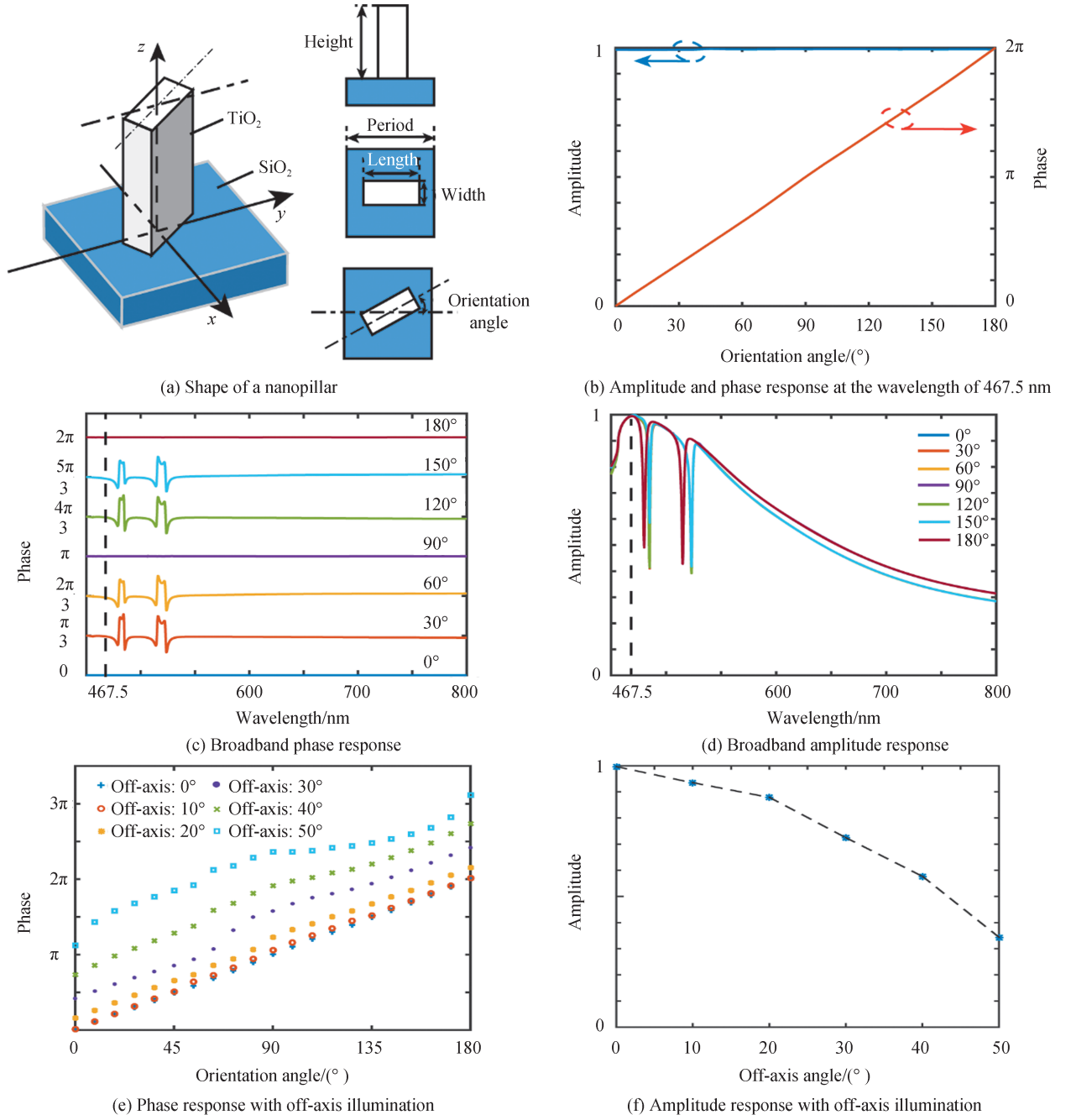
(a) Shape of a nanopillar

(b) Amplitude and phase response at the wavelength of 467.5 nm

(c) Broadband phase response

(d) Broadband amplitude response

(e) Phase response with off-axis illumination

(f) Amplitude response with off-axis illumination

Fig. 2　Details of the nanopillars

throughout the visible wavelength. The phase of the nanopillar with 0° orientation is set zero as the baseline. It can be seen that the relative phase shift is almost in linear relation with the orientation angle in the wavelength from 450 nm to 700 nm. The broadband amplitude responses of the proposed nanopillars are shown in Fig.2(d). Although the amplitude responses are different for the variation of the incident wavelengths, the cross-polarized amplitude nearly keeps constant with the change of the orientation angles. The broadband properties shown in Fig.2(c) and Fig.2(d) prove that the designed nanopillar can be operated in a broad wavelength range. The phase responses and average amplitude of the transmitted cross-polarization light for the off-axis illumination are shown in Fig.2(e) and (f). It can be seen that the phase shift produced by the nanopillars with an incident angle is similar to the normal incidence situation and basically follows a linear relation with the orientation angle of the unit structure (some deviations at large off-axis angles will not affect focus seriously because of the tolerance of the metalenses[24]). Therefore, metalenses with an off-axis angle can be designed based on the phase modulation relation of the TiO_2 nanopillars with normal incidence.

1.3　Metalens design

　　The metalenses are constructed with numerous nanopillars to modulate the phase of the transmitted light. In order to realize a planar ACE, the constructed metalenses focus the incident light with different inclination angles with an acceptable transmittance. According to the equal optical path principle, to focus the normally incident plane wave, the abrupt phase shift generated by nanopillars on the metalens should be a part-spherical shell[25, 26] (Fig. 3(a)) that satisfies this relation

$$\omega_{(x,y)} = 2\pi/\lambda \cdot (\sqrt{x^2+y^2+f^2} - f) \pm 2m\pi \tag{1}$$

where $\omega_{(x,y)}$ is the needed abrupt phase shift on different positions of the metalens, x and y are coordinates on the metalens, λ is the working wavelength (467.5 nm, which is also the wavelength of the Ar-Kr laser), f is the focal length (18 μm), m is an integer to make sure that the final value is within the range $0\sim2\pi$.

　　To counteract the effect of the incident light's inclination on the focusing performance, the wavefront of the transmitted light needs to remain a part-spherical shell. As is shown in Fig. 3(b), similar to the traditional method of adding a glass wedge to steer light beams[27], an off-axis phase shift $\delta_{(x,y)} = 2\pi/\lambda \cdot x \cdot \sin\alpha$ is introduced, where α is the off-axis angle. It is defined by the angle between the incident wave vector and the z-axis (here, the wave vector of the incident light is in the x-z plane). Thus, the needed phase distribution of the designed off-axis lens is determined by $\omega'_{(x,y)} = \omega_{(x,y)} + \delta_{(x,y)}$, as illustrated in Fig.3(c). The off-axis lens is coded by the nanopillars shown in Fig.2(a) with designed geometric phase relation, which can be described as

$$\theta_{(x,y)} = \omega'_{(x,y)}/2 = \pi/\lambda \cdot (\sqrt{x^2+y^2+f^2} - f) + \pi/\lambda \cdot x \cdot \sin\alpha \pm m\pi \tag{2}$$

where $\theta(x,y)$ is the nanopillars' orientation angle at different positions on the metalens. Fig. 3(d) shows an example of the metalens with the off-axis angle $\alpha = 30°$, focal length $f = 18$ μm and size length $d = 10.2$ μm. It is constructed with an array of 34×34 TiO$_2$ nanopillars. High-throughput lithography methods, such as deep-ultraviolet[28], can be utilized for the fabrication of the designed sample. A process can be used to manufacture the proposed metalens, it includes electron-beam lithography to create the lens pattern in the resist, atomic layer deposition to deposit the amorphous TiO$_2$ onto the developed resist, followed by controlled blanket reactive ion etching and stripping process[29]. The practical processing of the metalens array can be achieved

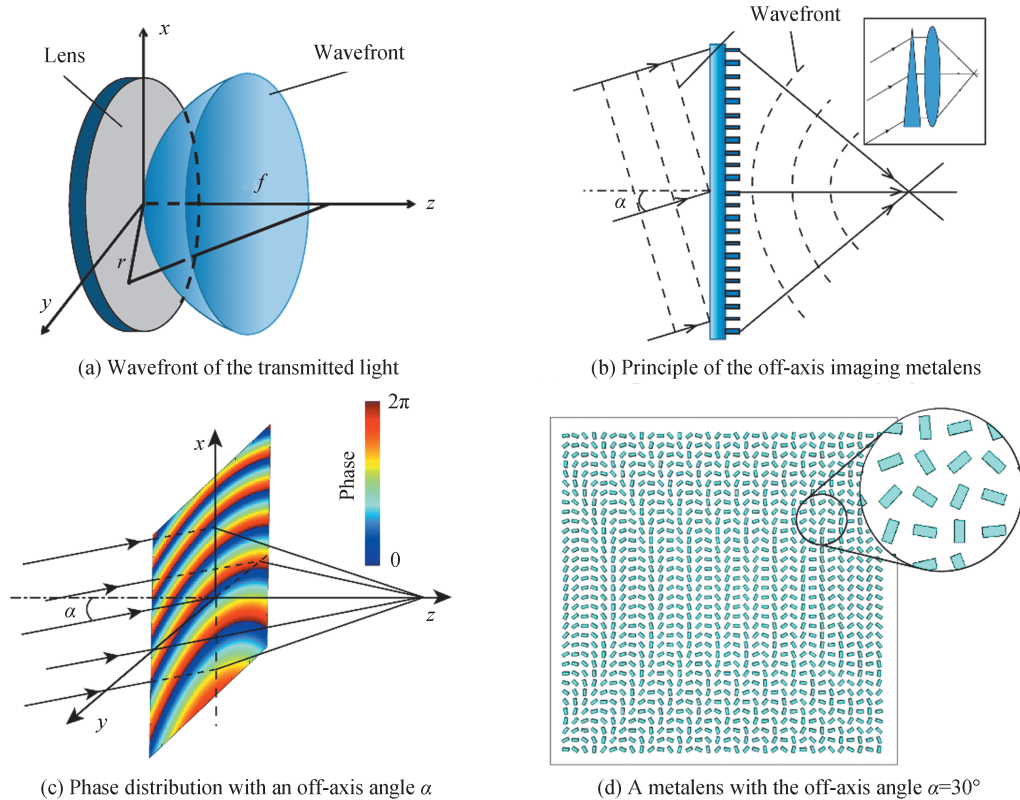
(a) Wavefront of the transmitted light

(b) Principle of the off-axis imaging metalens

(c) Phase distribution with an off-axis angle α

(d) A metalens with the off-axis angle $\alpha=30°$

Fig. 3　Details of the metalens

using similar methods[30].

2 Simulation

The FOV of a single metalens is very important for the imaging ability of the proposed planar ACE. The bigger it is, the less metalenses are needed to cover a large FOV. For metalenses, their FOVs are difficult to be acquired using the traditional glass-based formulas. In order to determine the FOV of the 0° off-axis metalens, the Point Spread Functions (PSFs) under different incidence angles are analyzed. Here, the electric fields of the metalenses are simulated and observed using the CST Microwave Studio. It should be noted that, because of the limited computing resources, direct calculation of the light field distribution at the focal plane is extremely difficult. To handle the problem, the near-field light field distribution on the plane of 0.5 μm above the metalens is extracted. Subsequently, the field distribution of the final focal spot is calculated using the vectorial angular spectrum theory[31-33]. The normalized intensity distribution of the transmitted electric field of the 0° off-axis metalens under 0°, 10° and 20° off-axis incidence is shown in Fig. 4. The produced FWHM under 0°, 10° and 20° off-axis angles are 0.74 μm, 0.77 μm and 0.89 μm, respectively. The FWHM under the 20° off-axis illumination increased 20.3% compared with the 0° situation. From the results, it can be concluded that the metalens is functional with the inclination angle of the incidence reaching as large as 20°. When the inclination angle is beyond such a value, the focal spot becomes less sharp and deformation becomes obvious, making it unable to focus properly. That is to say, the results indicate that the FOV of a single metalens reaches 40°.

To verify the feasibility of the proposed ACE structure, the optical performances of all the composed off-

(a) Thecross section of the transmitted field's intensity with 0° off-axis incidence

(b) Thecross section of the transmitted field's intensity with 10° off-axis incidence

(c) Thecross section of the transmitted field's intensity with 20° off-axis incidence

(d) The intensity distribution at the focal plane with 0° off-axis incidence

(e) The intensity distribution at the focal plane with 10° off-axis incidence

(f) The intensity distribution at the focal plane with 20° off-axis incidence
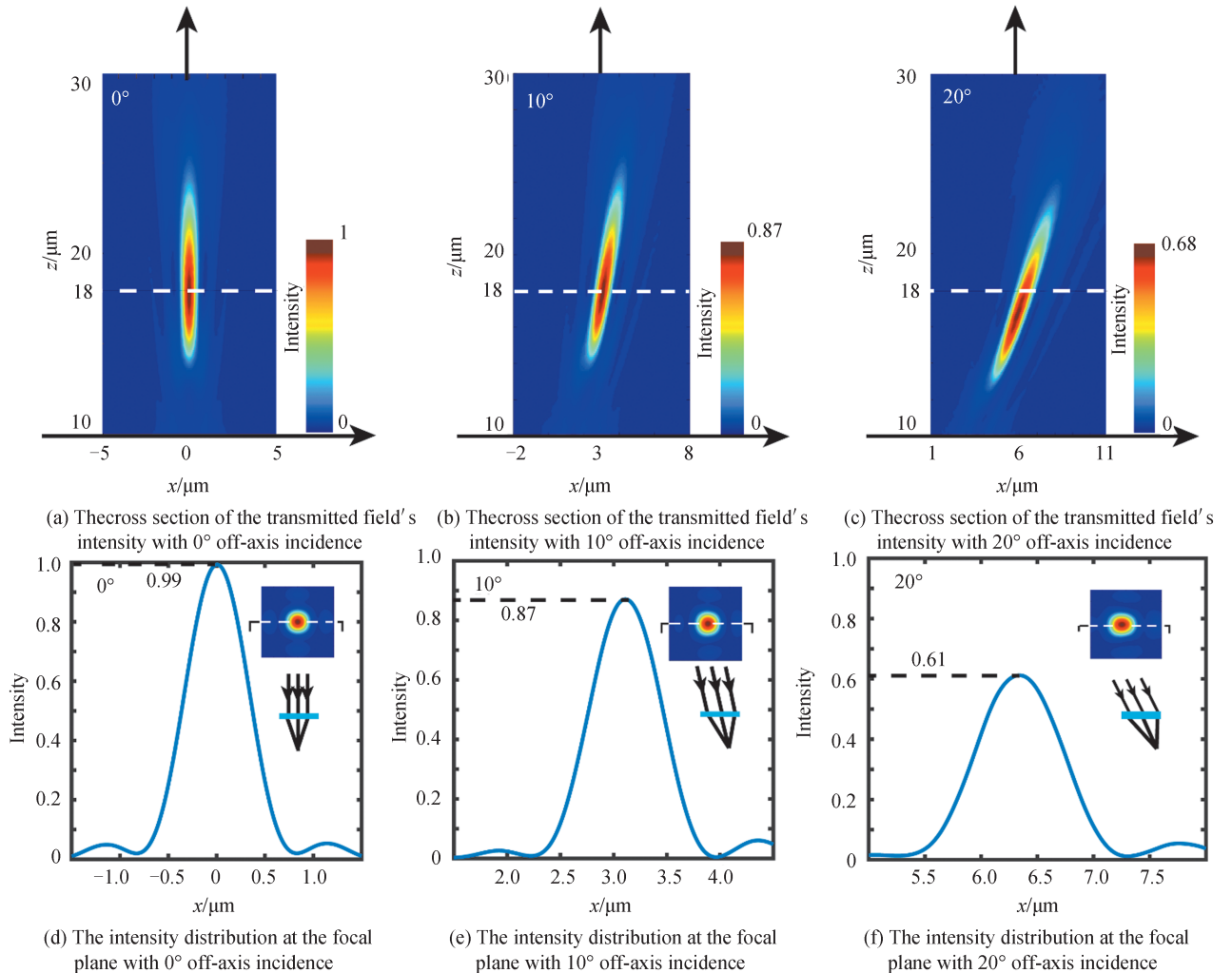
Fig. 4   The performance of the 0° off-axis metalens with inclined illumination. The intensities have been normalized with the maximum intensity in (a)

axis metalenses should be evaluated. However, although the metalenses are designed with different off-axis angles, their basic structures are similar. Here, three metalenses with the off-axis angles of 0°, 30° and 50° are chosen to verify the feasibility of the MA. For each metalens, the incident angle is set equal to its off-axis angle, making the emergent light normally focus onto the focal plane. The focusing intensity distribution and PSFs of the three metalenses are demonstrated in Fig.5(a)～(f). The FWHMs of the 0°, 30° and 50° off-axis metalenses are 0.74 μm, 0.74 μm and 0.75 μm, respectively. The FWHM of the 50° off-axis metalens is nearly the same as the 0° off-axis metalens, indicating that the imaging abilities of the metalenses are almost constant at large off-axis angles. The focusing efficiency is calculated by E_{foci}/E_{inci}, where E_{foci} is the energy within the first zero point, and E_{inci} is the overall incident energy. The focusing efficiencies of the 3 metalenses are 75.5%, 46.8% and 20.9%, respectively. The drop of the focusing efficiency at large off-axis angles indicate that fewer light beams are focused into the focal spot as the off-axis angle increases, and that the image quality and intensity may be reduced. However, the intensity differences for metalenses with large off-axis angles can be relieved through reverse-compensation in the post-treatment process.
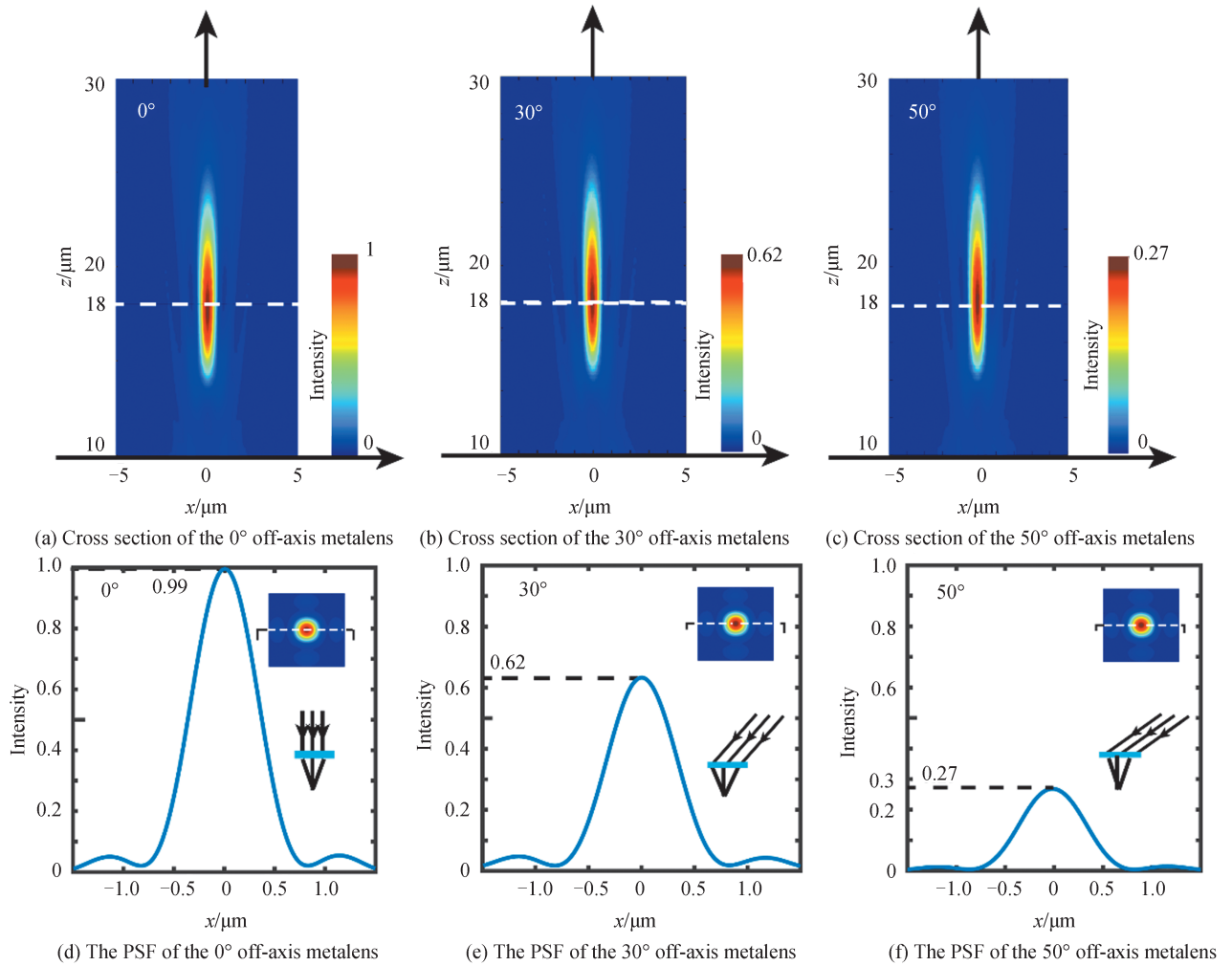

(a) Cross section of the 0° off-axis metalens

(b) Cross section of the 30° off-axis metalens

(c) Cross section of the 50° off-axis metalens

(d) The PSF of the 0° off-axis metalens

(e) The PSF of the 30° off-axis metalens

(f) The PSF of the 50° off-axis metalens

Fig. 5　The focusing performance of the 0°, 30° and 50° off-axis metalens. The intensities have been normalized with the maximum intensity in (a)

To verify the imaging ability, imaging simulation of all three metalenses are conducted using convolution computation. Here, two 1 μm-diameter points with the interval of 2 μm are taken as the object to generate the respective images. Fig. 6(a) shows the intensity distribution of the original 2-point object and its cross section (shown in the inset). Fig. 6(b), (c) and (d) showed the produced images and their cross sections (shown in the insets) for the 0°, 30° and 50° metalenses, respectively. It can be seen that despite some overlapping, the produced images of the 2-point object are discriminable, proving the off-axis metalenses' feasibility for imaging.
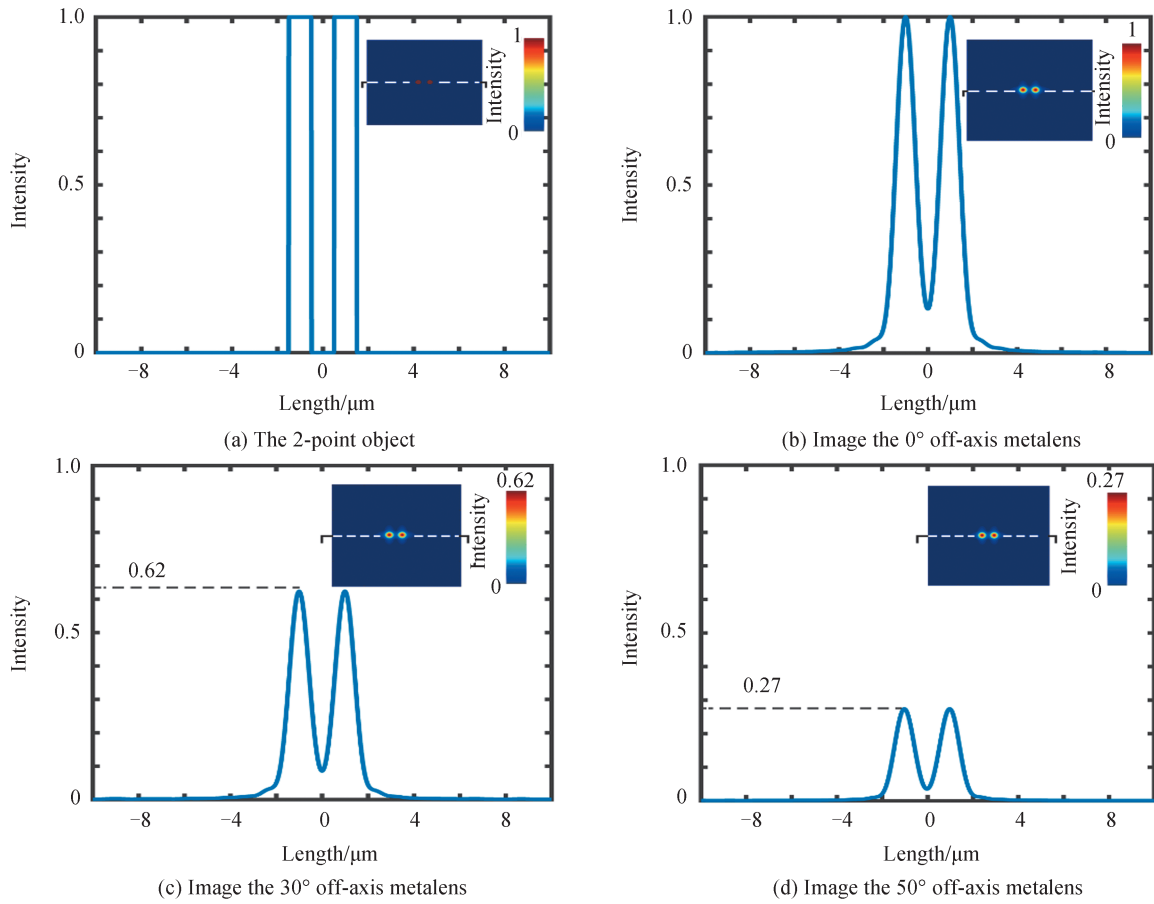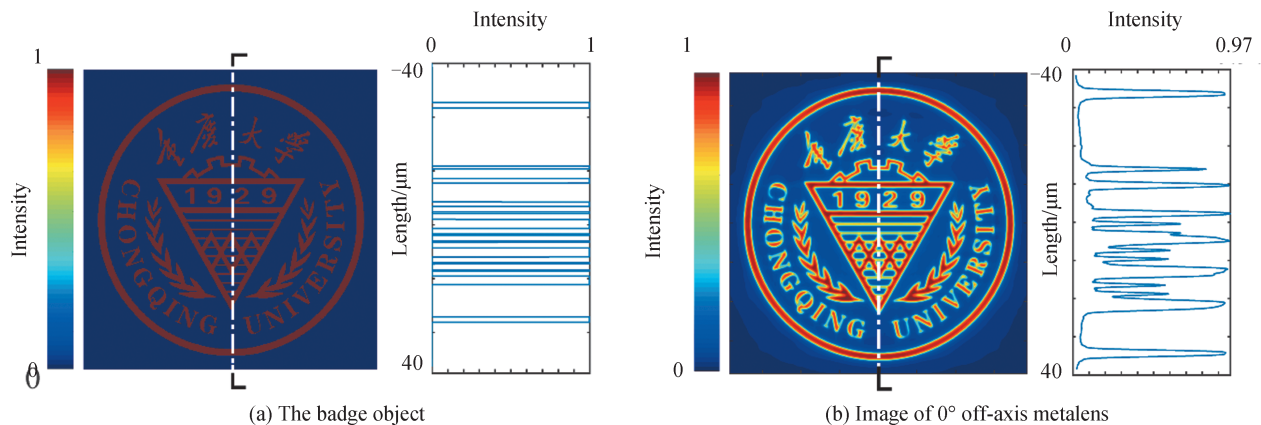
(a) The 2-point object

(b) Image the 0° off-axis metalens

(c) Image the 30° off-axis metalens

(d) Image the 50° off-axis metalens

Fig. 6　Imaging simulation with the two-point object. The intensities have been normalized with the maximum intensity in（b）

A more complicated picture（the badge of Chongqing University（Fig. 7（a））is chosen as the object to further verify the feasibility of the proposed scheme. The imaging performance of the 0°, 30° and 50° metalenses are shown in Fig. 7（b）～（d）. It can be seen that, although the image quality of the 50° off-axis metalens is mildly poorer, it can still be regarded as visible because the badge details remain recognizable after transmission. The reason for the degradation of the image quality is that the noise of the background is increased and the focusing efficiency is dropped with the increase of the incident angle. Although the imaging abilities of metalenses are influenced by the off-axis angle to some extent, it is good enough to produce a clear image of a complicated object.

A comparison of different ACE structures is shown in Table 1. Some parameters are compared including the surface type（planar/ 3D）, layer number（number of the optical device layers）, FOV（the overall FOV of the ACE）, size（the size of the whole ACE）, and overall height（the distance between the first layer of optical

(a) The badge object

(b) Image of 0° off-axis metalens

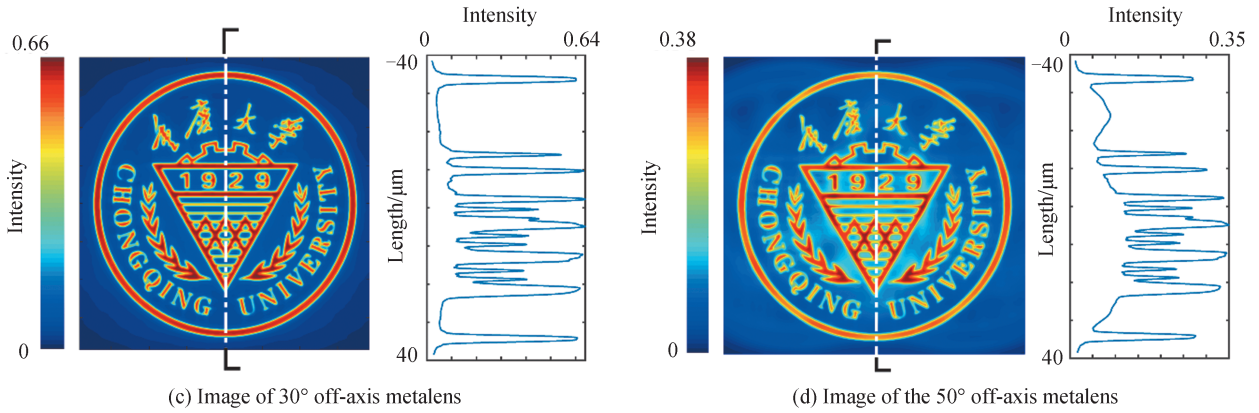(c) Image of 30° off-axis metalens

(d) Image of the 50° off-axis metalens

Fig. 7　Imaging simulation with the badge object. The intensities have been normalized with the maximum intensity in (b)

Table 1　The comparison of different ACE designs

ACE Design	Surface	Layer number	FOV	Size/μm	Overall height
This work	Planar	1	140°×140°	165×165	18.6 μm
3-layer planar ACE[12]	Planar	3	70°×10°	4500×500	2 mm
Prism-based planar ACE[11]	Planar	4	30°×30°	—	24.8 mm
Flexible zoom ACE[17]	3D	1	—	Diameter=8 660	2.283 mm
3D ACE using laser scanning[34]	3D	1	90°×90°	Diameter=84	20 μm
3D ACE using polymerization[35]	3D	2	107.48°×97.97°	30×30	15 μm

device and the image plane). It can be seen that the proposed metalens-based planar ACE obtains a large FOV with a single-layered planar structure. Due to the compact structure of metalenses, the geometric dimensions of the ACE are also extremely small.

3　Conclusion

In this work, a scheme to realize a planar ACE with a large FOV is proposed. It is composed of a transparent SiO_2 substrate to hold the whole structure, a receiver to collect the produced images, and a metalens array, which uses metalenses in this work to image different portions of the object field. Although a single metalens covers a limited FOV, the combined image of the metalenses cover a large FOV with proper arrangement of the off-axis angles of the metalenses, which reaches as large as $140^o \times 140°$ in this work. Importantly, because the off-axis angle is embedded within the structure of the metalenses, they do not require additional components to aim for different fields. The metalenses and their produced subimages both lie on a planar plane, making it beneficial for designing and manufacturing as no complicated curving process or any intermediate devices are required. In practical use, the intensity difference between the subimages should be compensated in the post-treatment process to avoid abrupt change of local brightness. Combined with the fast development of metasurfaces, the metasurfaces-based ACEs allow for not only large FOV and compact size, but also color imaging ability[36] and polarization sensitivity[37]. With advantages on small size and multiple-imaging, the proposed ACE has wide utilization in micro security camera, medical inspection, and distance estimation.

References

[1]　FISCHER S, MULLER C H G, MEYER-ROCHOW V B. How small can small be: The compound eye of the parasitoid wasp Trichogramma evanescens (Westwood, 1833) (Hymenoptera, Hexapoda), an insect of 0.3-to 0.4-mm total body size[J]. Visual Neuroscience, 2011, 28(4): 295-308.

[2]　STOLLBERG K, BRUCKNER A, DUPARRE J, et al. The Gabor superlens as an alternative wafer-level camera approach inspired by superposition compound eyes of nocturnal insects[J]. Optics Express, 2009, 17(18): 15747-15759.

[3]　FRIEDRICH M, BENZER S. Divergent decapentaplegic expression patterns in compound eye development and the

evolution of insect metamorphosis[J]. Journal of Experimental Zoology, 2000, 288(1): 39-55.

[4] ZHU Lin, GAO Yuanyuan, HU Xinyu, et al. Progress in femtosecond laser fabrication of artificial compound eye[J]. Chinese Science Bulletin, 2019, 64(12): 1254-1267.

[5] JUNG H, JEONG K H. Microfabricated ommatidia using a laser induced self-writing process for high resolution artificial compound eye optical systems[J]. Optics Express, 2009, 17(17), 14761-14766.

[6] KUO Wenkai, KUO Guanfu, LIN S Y, et al. Fabrication and characterization of artificial miniaturized insect compound eyes for imaging[J]. Bioinspiration & Biomimetics, 2015, 10(5): 056010.

[7] ZHANG Shuqing, ZHOU Luyang, XUE Changxi, et al. Design and simulation of a superposition compound eye system based on hybrid diffractive-refractive lenses[J]. Applied Optics, 2017, 56(26): 7442-7449.

[8] FALLAH H R, KARIMZADEH A. Design and simulation of a high-resolution superposition compound eye[J]. Journal of Modern Optics, 2007, 54(1): 67-76.

[9] LEEM J W, SONG Y M, YU J S. Biomimetic artificial Si compound eye surface structures with broadband and wide-angle antireflection properties for Si-based optoelectronic applications[J]. Nanoscale, 2013, 5(21): 10455-10460.

[10] LI Lun, HAO Yongping, XU Jiulong, et al. The design and positioning method of a flexible zoom artificial compound eye [J]. Micromachines (Basel), 2018, 9(7): 319.

[11] DRUART G, GUÉRINEAU N, HAÏDAR R, et al. Demonstration of an infrared microcamera inspired by xenos peckii vision[J]. Applied Optics, 2009, 48(18): 3368-3374.

[12] DUPARRE J, SCHREIBER P, MATTHES A E, et al. Microoptical telescope compound eye[J]. Optics Express, 2005, 13(3): 889-903.

[13] KHORASANINEJAD M, SHI Z, ZHU A Y, et al. Achromatic metalens over 60 nm bandwidth in the visible and metalens with reverse chromatic dispersion[J]. Nano Letter, 2017, 17(3): 1819-1824.

[14] MA Xiaoliang, PU Mingbo, LI Xiong, et al. All-metallic wide-angle metasurfaces for multifunctional polarization manipulation[J]. Opto-Electronic Advances, 2019, 2(3): 180023.

[15] GUO Jingying, WANG Teng, QUAN Baogang, et al. Polarization multiplexing for double images display[J]. Opto-Electronic Advances, 2019, 2(7): 180029.

[16] ZHELUDEV N I, KIVSHAR Y S. From metamaterials to metadevices[J]. Nature Materials, 2012, 11(11): 917-924.

[17] ZHANG Hao, LI Lei, MCCRAY D L, et al. Development of a low cost high precision three-layer 3D artificial compound eye[J]. Optics Express, 2013, 21(19): 22232-22245.

[18] KARIMZADEH A. Optical design of high resolution concave superposition compound eye[J]. Osa Continuum, 2019, 2(11): 3044-3049

[19] DUPARRE J, DANNBERG P, SCHREIBER P, et al. Thin compound-eye camera[J]. Applied Optics, 2005, 44(15): 2949-2956.

[20] HERMON S, MA A, YUE Fuyong, et al. Metasurface hologram for polarization measurement[J]. Optics Letters, 2019, 44(18): 4436-4438.

[21] CHEN B H, WU P C, SU V C, et al. GaN metalens for pixel-level full-color routing at visible light[J]. Nano Letters, 2017, 17(10): 6345-6352

[22] MUELLER J P B, RUBIN N A, DEVLIN R C, et al. Metasurface polarization optics: independent phase control of arbitrary orthogonal states of polarization[J]. Physical Review Letters, 2017, 118(11): 113901.

[23] DEVLIN R C, KHORASANINEJAD M, CHEN W T, et al. Broadband high-efficiency dielectric metasurfaces for the visible spectrum[J]. Proceedings of the National Academy of Sciences, 2016, 113(38): 10473-10478.

[24] ZHANG Xiaohu, JIN Jinjin, PU Mingbo, et al. Ultrahigh-capacity dynamic holographic displays via anisotropic nanoholes [J]. Nanoscale, 2017, 9(4): 1409-1415.

[25] CHEN Deli, WANG Junjie, QI Yongle, et al. Polarization-insensitive dielectric metalenses with different numerical apertures and off-axis focusing characteristics[J]. Journal of the Optical Society of America B, 2020, 37(12): 3588-3595.

[26] KHORASANINEJAD M, CHEN W T, OH J, et al. Super-dispersive off-axis meta-lenses for compact high resolution spectroscopy[J]. Nano Letters, 2016, 16(6): 3732-3737.

[27] DUNCAN, BOS B, SERGAN P, et al. Wide-angle achromatic prism beam steering for infrared countermeasure applications[J]. Optical Engineering, 2003, 42(4): 1038 – 1047.

[28] PARK J S, ZHANG Shuyan, SHE A, et al. All-glass, large metalens at visible wavelength using deep-ultraviolet projection lithography[J]. Nano Letters, 2019, 19(12): 8673-8682.

[29] KHORASANINEJAD M, CHEN W T, DEVLIN R C, et al. Metalenses at visible wavelengths: Diffraction-limited focusing and subwavelength resolution imaging[J]. Science, 2016, 352(6290): 1190-1194.

[30] FAN Zhibin, QIU Haoyang, ZHANG Hanle, et al. A broadband achromatic metalens array for integral imaging in the visible[J]. Light: Science & Applications, 2019, 8: 67.

[31] TANG Dongliang, CHEN Long, LIU Jianjun. Visible achromatic super-oscillatory metasurfaces for sub-diffraction

focusing［J］. Optics Express，2019，27(9)：12308-12316.

［32］ TANG Dongliang，LIU Jia，CHEN Long，et al. Reflective plasmonic super-oscillatory metasurfaces with simultaneous phase and amplitude controls for sub-diffraction focusing［J］. Journal of Physics D：Applied Physics，2020，53(15)：154001.

［33］ FU Rao，LI Zile，ZHENG Guoxing，et al. Reconfigurable step-zoom metalens without optical and mechanical compensations［J］. Optics Express，2019，27(9)：12221-12230

［34］ WU Dong，WANG Jiannan，NIU Ligang，et al. Bioinspired Fabrication of high-quality 3D artificial compound eyes by voxel-modulation femtosecond laser writing for distortion-free wide-field-of-view imaging ［J］. Advanced Optical Materials，2014，2(8)：751-758.

［35］ LIN Jieqiong，KAN Yudi，JING Xian，et al. Design and fabrication of a three-dimensional artificial compound eye using two-photon polymerization［J］. Micromachines，2018，9(7)：336.

［36］ COLBURN S，ZHAN A，MAJUMDAR A. Metasurface optics for full-color computational imaging ［J］. Science Advances，2018，4(2)：eaar2114

［37］ MIYATA M，NAKAJIMA M，HASHIMOTO T. Compound-eye metasurface optics enabling a high-sensitivity，ultra-thin polarization camera［J］. Optics Express，2020，28(7)：9996-10014.